Geophys. J. Int. (1990) **100**, 327–336

Long-wavelength *S*-wave velocity structure throughout the mantle

Toshiro Tanimoto
Seismological Laboratory, 252-21, California Institute of Technology, Pasadena, CA 91125, USA

Accepted 1989 July 15. Received 1989 June 9; in original form 1988 June 30

SUMMARY

Long-wavelength *S*-wave velocity anomalies are obtained for the entire mantle by inverting 6000 long-period (40–100 s) *SH* body waves and 1000 long-period (100–500 s) Love waves. In the shallow mantle, the patterns of fast and slow velocity anomalies correlate well with age and tectonics. In the depth range of 400–1000 km, we find two antipodal fast velocity anomalies, one in the western Pacific and the other in South America. They form a fairly strong $l = 2$ anomaly. Moreover the $l = 2$ anomaly is the largest spherical harmonic component throughout the entire mantle except for in the layer of 1000–1300 km depth. A fast-velocity anomaly near the Caribbean, previously reported by several other investigators, is found between the depths of 1000 and 1300 km. With diminishing amplitudes, it can be traced to Canada and the Aleutians and may be related to old subducted slabs. In the same depth interval, similar size anomalies can be found in the middle of the Pacific and in the Indian Ocean. These could be checked by more detailed studies to judge the reliability of this study. Heterogeneity power has a peak at the surface and a secondary peak at the bottom of the mantle (D″), consistent with the existence of chemical and/or thermal boundary layers. At the base of the mantle we also find a fast-velocity anomaly which surrounds the Pacific Ocean. This feature has been found by other researchers previously, but its interpretation is difficult due to the trade-off between velocity anomaly and (core–mantle) boundary deformation.

Key words: Earth's mantle, lateral heterogeneity, *S*-wave velocity.

1 INTRODUCTION

With the accumulation of digital seismograph network data, we can continually improve our understanding of the interior structure of the Earth. During the last five or six years, we have seen advances in Earth structure study, beginning with shallow regions and progressing to the deep interior (e.g. Woodhouse & Dziewonski 1984; Nataf, Nakanishi & Anderson 1984, 1986; Tanimoto 1986, 1987, 1988; Dziewonski & Woodhouse 1987). Methods of studying Earth structure have included normal mode (Ritzwoller, Masters & Gilbert 1986; Giardini, Li & Woodhouse 1987), surface wave (Nataf *et al.* 1986; Tanimoto 1986) and long-period body wave analyses (Dziewonski & Woodhouse 1987). However most of the results so far are relatively low in resolution, representing averaged velocity over (lateral) range of a few thousand km (Tanimoto 1985). This will be improved by probing the interior with shorter period waves. This study is one such effort to improve the previous structures by using long-period body waves. The probing wavelength is about a factor of two to three shorter than previous surface wave studies. Also, because of the deep turning point of body waves, this study provides better depth resolution especially in the lower mantle.

The main content of this paper is the results of a transverse component waveform study for the *S*-wave velocity structure of the entire mantle. We will invert long-period body waves (40–100 s) as well as long-period surface waves (100–500 s) to recover long-wavelength *S*-wave velocity anomalies (angular order 1–6) in the mantle. Most previous studies have been carried out using arrival times from ISC (International Seismological Center). This study, along with the work by Woodhouse as reported in Dziewonski & Woodhouse (1987), represents one of the first studies to obtain the structure of the lower mantle using waveform inversions. The entire mantle structure is recovered by fitting the waveforms of deep turning *S*-, *SS*-, *SSS*-, . . . , waves as well as Love waves.

In the following, we describe the data set (Section 2), the resulting images and some of their features (Section 3) and limitations of the method used for inversion (Section 4). We will describe the method for inversion, but since details were given previously (Woodhouse 1983; Tanimoto 1984a, 1987; Woodhouse & Dziewonski 1984), we will do so briefly.

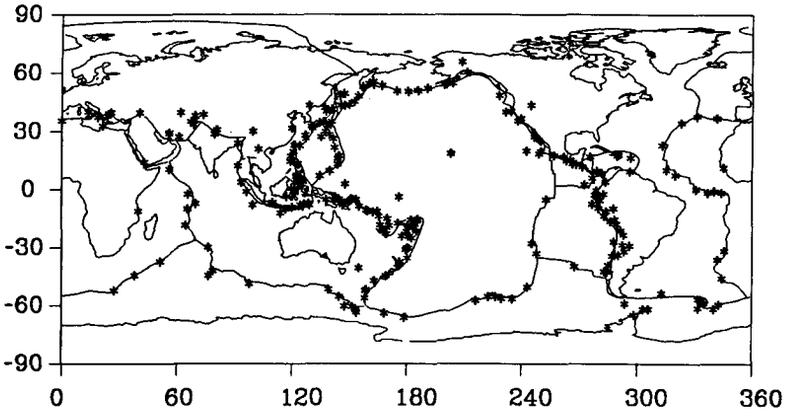

Figure 1. Earthquake distribution; location of 271 earthquakes used for inversion.

2 DATA AND METHOD

The body wave portion of the data consists of approximately 6000 transverse-component seismograms from the Global Digital Seismograph Network (GDSN). All long-period seismograms from the GDSN tapes (including SRO, ASRO, RSTN and DWWSSN data) were filtered between periods of 40 and 100 s and sampled every 10 s. These filtered waveform data contain *S*, *SS*, *SSS*, . . . , up to the arrival time of Love waves. These body wave data are supplemented by long-period Love wave data (100–500 s), previously used for upper mantle studies (Tanimoto 1988). Although the body waves, such as *SS*, *SSS*, . . . , give us good coverage in the shallow mantle, the addition of surface wave data insures fairly complete, uniform coverage in the upper mantle which results in better resolution in the lower parts of the mantle.

The number of earthquakes used in the inversion is 271. Locations are shown by asterisks in Fig. 1. In order to obtain a good path coverage over the entire Earth, all earthquakes were binned in $5° \times 5°$ cells and selected one earthquake from each cell. In cases where there were earthquakes with markedly different depths in the same cell, such as 30 and 600 km, two earthquakes from one cell were used.

The waveform inversion method adopted was based on normal mode theory which is similar to that used by Woodhouse & Dziewonski (1984). The exact formulae used are given in Tanimoto (1988, equations 3 and 6). Seismograms are assumed to be affected by the average structure between earthquakes and seismic stations. This method corresponds to a low-order perturbation theory (e.g. Mochizuki 1986), and is more suitable for surface waves. It would be improved by a more elaborate theory, but considering economy of computation, the current approach seems to be a good compromise at the present time. Also, for retrieval of long-wavelength anomalies, this method is presumably appropriate. We will consider some deficiencies of this method in Section 4.

Transverse-component theoretical seismograms are computed by adding approximately 1500 torodidal modes. The modes were generated for the Earth model PREM (isotropic version, Dziewonski & Anderson 1981) which is also the starting model for the inversion. Most of the modes between the period range of 40 and 100 s were summed. The modes which were dropped are the ones below the angular degree of $l = 40$, because they do not contribute to body waves significantly. These effects were examined carefully before dropping these long-wavelength modes.

For body waves, the time portion of data inverted is from the *S*-wave arrival time to just before the arrival time of the Love wave. Figs 2(a) and (b) show two examples of data and synthetics. In each figure, the top trace is the data, the second is the synthetic seismogram and the traces below them are time series generated by various overtone branches which have appreciable contributions. The four wave packets seen in Fig. 2(a) are *S* (diffracted), *SS*, *SSS* and *SSSS*. Since the distance range is such that *S*-waves are diffracted waves, these have relatively small amplitudes. These direct *S*-waves are the source of information for the lowermost mantle and thus are very important.

For the surface wave part, we used the long-period waveform of Love waves filtered between 100 and 500 s. The number of paths used for Love waves is approximately 1100. This part of the data is the same as in Tanimoto (1988) and details are given in that paper.

3 RESULTS

3.1 *S*-wave velocity maps

The mantle was divided into 11 shells and the data solved for $\delta\beta/\beta$ in each shell, where β is the *S*-wave velocity and $\delta\beta$ is its perturbation. Radial locations of boundaries are given in Table 1. In each shell, $\delta\beta/\beta$ is assumed to be independent of the radius r, and is expanded in terms of spherical harmonics up to $l = m = 6$ by

$$\left(\frac{\delta\beta}{\beta}\right)_i = \sum_{l=0}^{6} \sum_{m=-l}^{l} b^i_{lm} Y^m_l(\theta, \varphi),$$

where i denotes the ith shell.

Formulae for inversion are the same as equations (3) and (6) in Tanimoto (1988). Using these formulae, we inverted the waveforms for the coefficients b^i_{lm}. There are 539 (49×11) unknowns in this problem. We adopted a simple damped least-squares approach as in previous contributions (Tanimoto 1984b, 1987, 1988).

The variance reduction obtained by the model presented

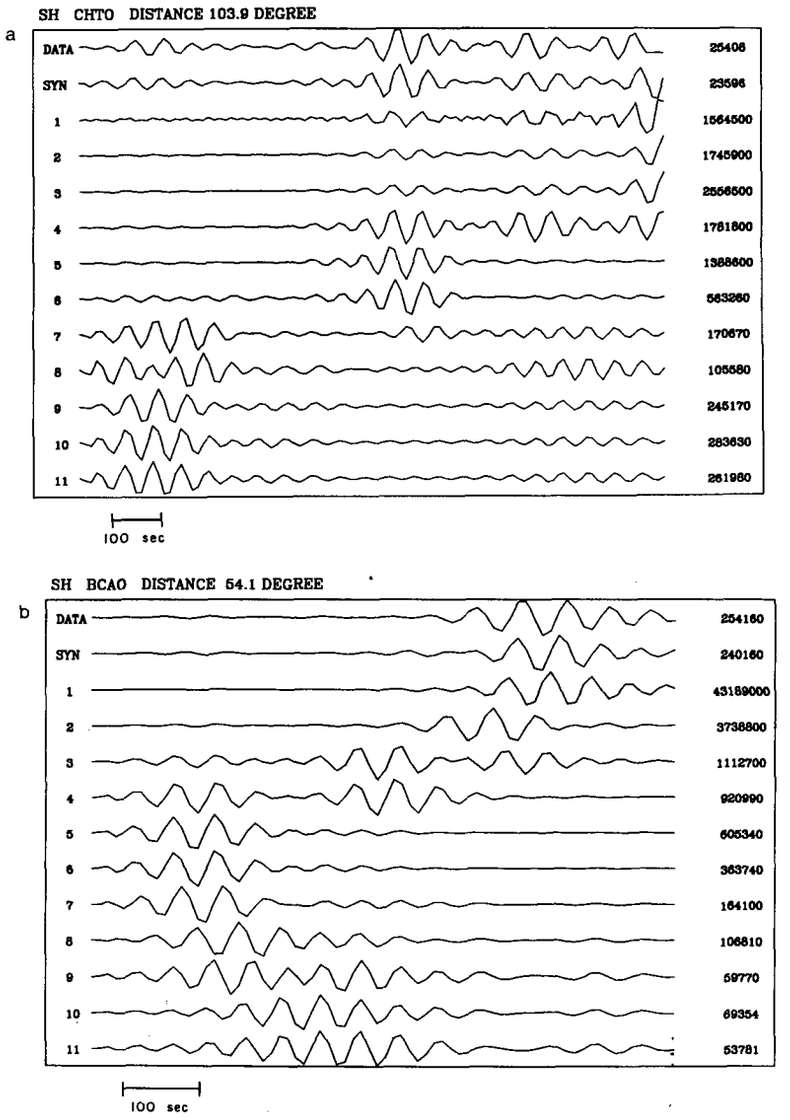

Figure 2. Data (top) and synthetic seismograms (second trace) for an elliptical earth model. The earth model, PREM, was used for computation of synthetic seismograms. Traces from the third row to the bottom are synthetics for various overtone branches, but the branch number does not necessarily correspond to the conventional definition. The branches that have large contributions to body waves are shown here. Four major wave packets in (a) from left to right are *S* (diffracted), *SS*, *SSS* and *SSSS*. The first three are seen in (b). The numbers on the right are maximum count of digital counts for each trace.

below is 18 per cent. This is lower relative to surface wave inversions previously performed (e.g. Woodhouse & Dziewonski 1984; Tanimoto 1987, 1988), which generally yielded about 30 per cent of variance reduction. It indicates some difficulties in retrieving 3-D structure information from body waves. This is in fact expected from the original seismograms; it is generally true that effects of heterogeneity in the data are much smaller for deep turning body waves than for surface waves. This becomes apparent when we compare arrival times of various wave packets (see for example fig. 3 in Woodhouse & Dziewonski 1984). We believe that this is related to the fact that heterogeneity is smaller in the lower mantle than near the surface; this is discussed below. For such cases, (since signal due to heterogeneity is small in the data), the variance reduction may also become small due to the dominance of random noise.

Table 1. Top and bottom radius of each layer (km).

layer	top	bottom
1	6371.	6151.
2	6151.	5971.
3	5971.	5701.
4	5701.	5349.
5	5349.	5087.
6	5087.	4816.
7	4816.	4555.
8	4555.	4283.
9	4283.	4012.
10	4012.	3741.
11	3741.	3480.

Figure 3(a–k) shows our results of *S*-wave velocity variation in 11 layers. Shaded regions denote faster velocity than average, at each depth, and white regions denote slower than average velocity. Contour interval is 0.5 per cent ($\delta\beta/\beta$). Coefficients for b^i_{lm} are given in Table 2. We

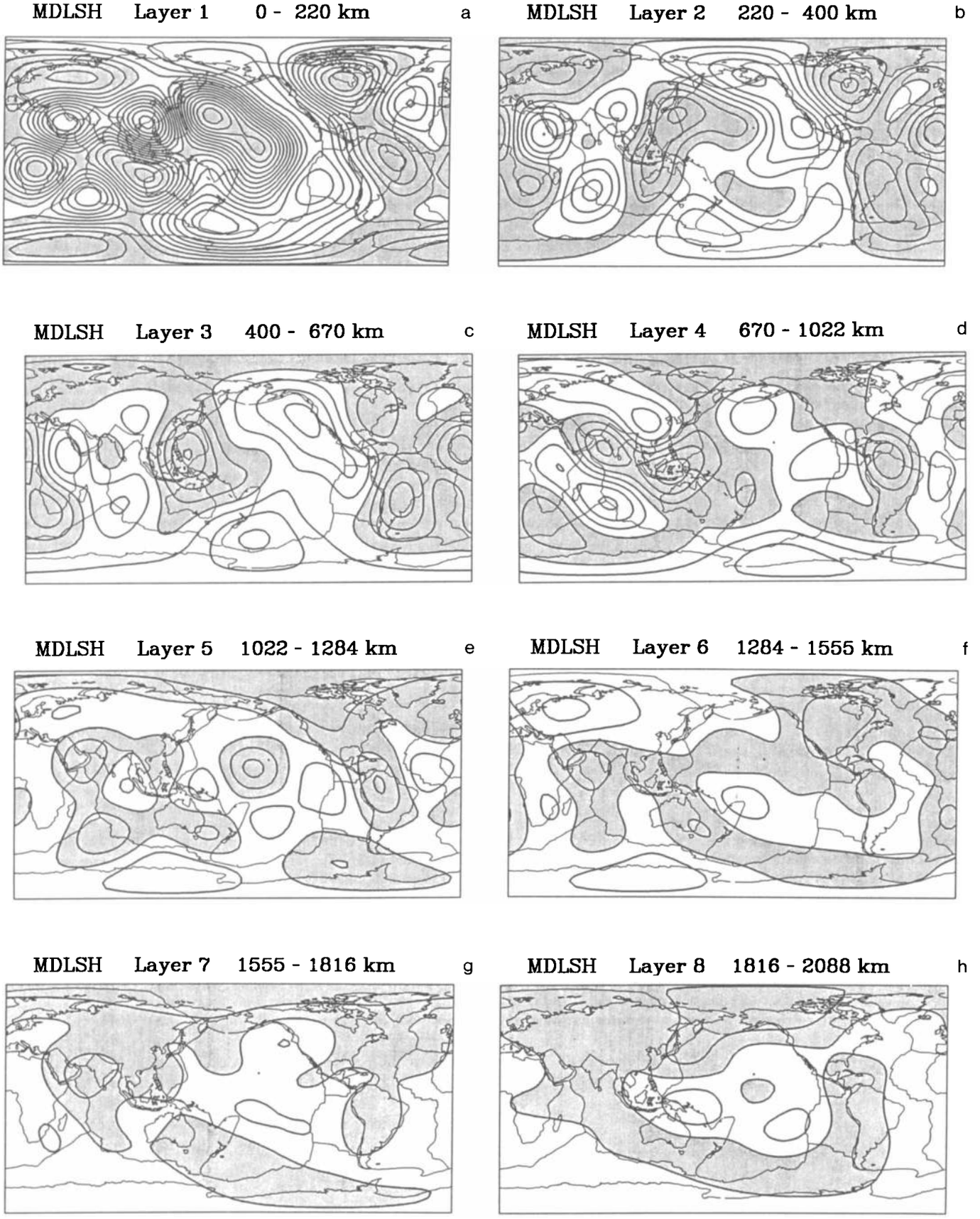

Figure 3. *S*-wave velocity variations in 11 layers. Dark regions are fast-velocity regions and white regions are slow. Contour interval is 0.5 per cent.

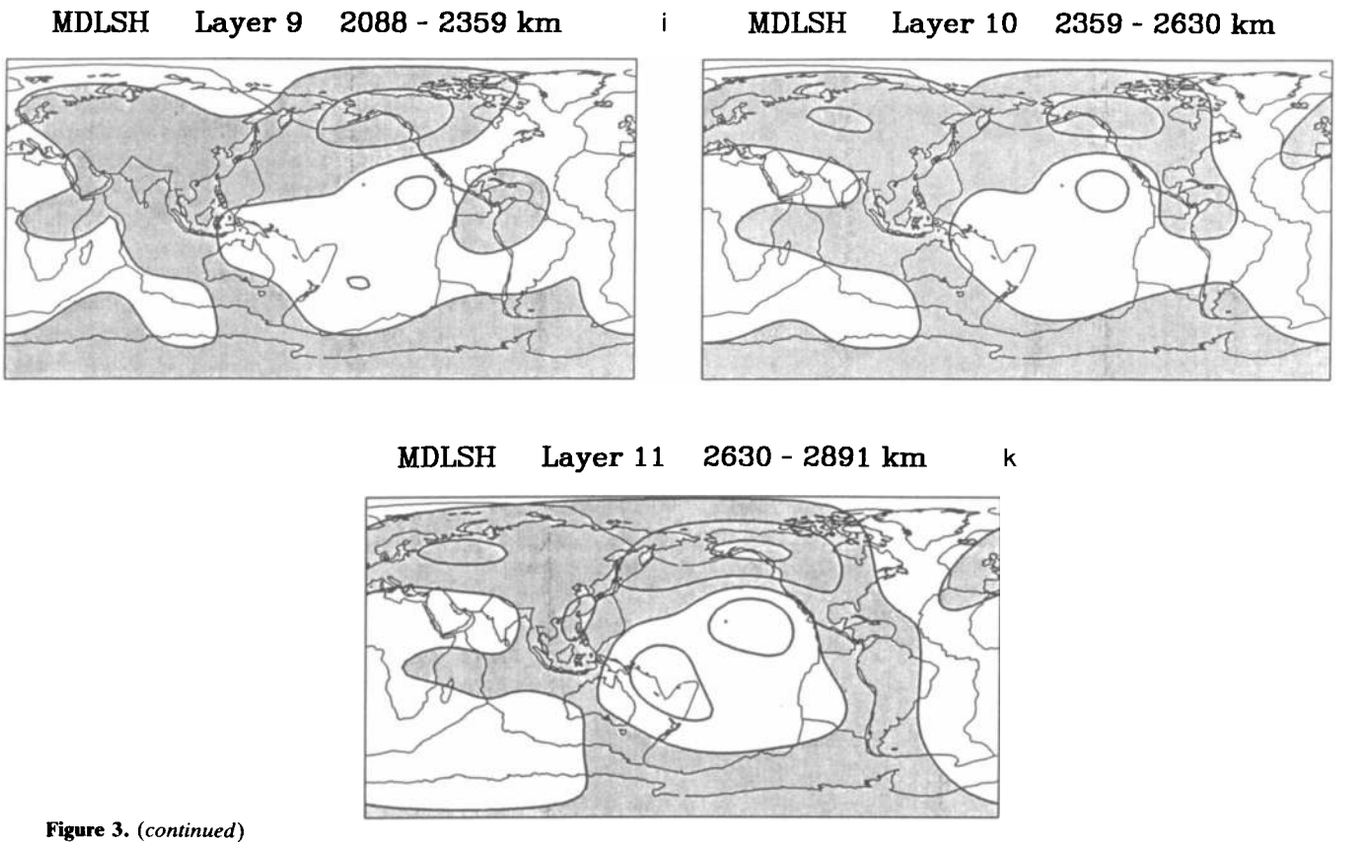

Figure 3. (*continued*)

Table 2. Spherical harmonic coefficients of $\delta\beta/\beta$ for each layer. Depth range of each layer is given in Table 1.

l	m		1	2	3	4	5	6	7	8	9	10	11
0	0	C	-0.141	0.533	0.146	0.082	-0.322	-0.097	-0.036	0.074	0.040	0.070	0.199
1	0	C	0.114	0.052	0.053	0.013	0.062	0.028	0.099	0.102	0.065	0.062	0.117
1	1	C	0.028	0.233	0.222	-0.067	0.011	0.011	0.006	-0.009	-0.005	-0.007	0.009
1	1	S	0.068	-0.001	0.035	0.067	0.007	-0.044	0.060	0.031	0.046	0.050	0.026
2	0	C	-0.208	-0.034	-0.154	-0.130	0.024	-0.081	0.069	0.091	0.064	0.085	0.127
2	1	C	-0.390	0.011	-0.084	-0.012	-0.047	-0.030	0.057	-0.021	-0.078	-0.026	-0.058
2	1	S	-0.378	0.071	0.117	0.015	-0.067	-0.116	0.047	0.051	0.021	0.018	0.037
2	2	C	0.486	0.212	0.135	-0.046	-0.067	-0.053	-0.085	-0.091	-0.051	-0.074	-0.127
2	2	S	-0.141	-0.433	-0.467	-0.187	0.002	-0.020	-0.066	0.004	-0.033	-0.053	-0.086
3	0	C	0.018	0.062	0.114	0.033	0.028	-0.054	0.007	0.015	-0.039	-0.026	-0.022
3	1	C	0.386	0.184	0.204	0.085	-0.003	-0.040	-0.058	-0.127	-0.063	-0.049	-0.107
3	1	S	-0.010	-0.080	-0.049	-0.074	-0.075	-0.147	-0.035	-0.012	-0.009	-0.036	-0.035
3	2	C	0.170	0.015	-0.013	-0.070	0.006	-0.040	-0.037	0.030	0.035	0.011	0.021
3	2	S	0.017	-0.130	-0.091	0.045	0.062	0.028	0.024	0.038	0.032	0.007	-0.008
3	3	C	-0.241	0.029	0.073	-0.038	-0.163	0.016	-0.077	-0.077	-0.029	0.001	-0.003
3	3	S	-0.168	0.008	0.062	0.074	-0.006	0.004	-0.006	0.019	0.019	0.023	0.049
4	0	C	0.311	-0.019	0.042	0.028	-0.012	-0.023	0.025	-0.021	0.001	0.005	-0.012
4	1	C	0.168	0.094	-0.020	-0.168	0.019	0.006	0.010	-0.001	-0.008	0.006	-0.002
4	1	S	0.201	-0.045	-0.061	-0.109	-0.008	-0.030	-0.005	0.018	-0.011	0.019	0.015
4	2	C	-0.227	-0.083	-0.132	0.082	-0.067	0.049	0.053	0.035	0.006	-0.011	0.033
4	2	S	-0.150	0.005	0.006	0.140	0.019	-0.029	-0.041	-0.026	0.032	0.028	0.031
4	3	C	-0.410	-0.072	0.004	-0.077	-0.008	0.002	-0.005	-0.001	-0.031	-0.004	0.021
4	3	S	0.309	0.083	-0.011	-0.025	-0.008	-0.012	-0.020	0.015	0.000	-0.007	0.026
4	4	C	0.044	0.011	-0.048	-0.018	0.009	0.026	0.003	0.023	0.021	0.007	0.004
4	4	S	0.401	0.117	0.049	0.100	0.096	-0.086	-0.030	0.051	0.023	0.028	0.059
5	0	C	-0.422	-0.032	0.055	0.112	0.081	0.061	0.064	0.049	-0.031	-0.046	-0.060
5	1	C	0.303	0.173	-0.041	-0.061	-0.002	-0.011	-0.004	0.008	0.014	0.003	-0.016
5	1	S	0.035	0.043	0.050	0.124	-0.120	-0.071	-0.028	-0.059	-0.046	-0.011	-0.016
5	2	C	-0.207	-0.157	0.011	0.047	0.020	-0.033	-0.012	0.008	-0.001	-0.015	0.014
5	2	S	0.027	0.057	0.030	-0.036	-0.074	-0.083	-0.061	0.007	0.070	0.065	0.093
5	3	C	0.004	-0.038	0.016	0.098	0.043	0.014	-0.027	-0.014	-0.007	0.009	0.004
5	3	S	0.325	0.126	0.143	0.140	0.002	-0.009	-0.004	0.047	-0.004	0.007	0.023
5	4	C	0.380	0.171	0.088	-0.028	0.004	0.015	-0.015	-0.021	0.004	0.037	0.045
5	4	S	-0.353	-0.138	-0.088	-0.134	0.062	-0.001	-0.022	-0.051	0.007	0.007	-0.031
5	5	C	0.091	0.103	0.130	0.101	0.066	0.079	0.033	0.034	0.004	-0.006	0.006
5	5	S	0.165	-0.094	-0.035	0.014	-0.070	-0.035	0.001	-0.022	-0.025	-0.029	-0.036
6	0	C	-0.134	0.025	0.019	-0.036	0.041	0.009	0.029	-0.014	-0.039	-0.043	-0.061
6	1	C	-0.100	0.009	0.014	-0.037	-0.094	-0.047	-0.046	-0.049	0.010	-0.002	0.001
6	1	S	-0.244	-0.011	0.024	-0.004	0.052	0.069	0.025	-0.019	-0.005	0.008	0.020
6	2	C	-0.369	-0.161	-0.026	-0.095	0.010	-0.046	0.010	0.020	-0.011	-0.016	0.003
6	2	S	0.191	0.001	-0.009	-0.105	0.034	0.000	0.007	0.085	0.053	0.054	0.067
6	3	C	0.080	-0.041	-0.057	0.102	0.082	0.044	-0.019	0.012	0.021	0.030	0.020
6	3	S	0.190	0.231	0.079	0.014	-0.033	0.006	0.013	0.000	-0.043	-0.037	-0.027
6	4	C	0.152	-0.046	-0.007	-0.027	0.020	0.046	0.040	-0.003	-0.026	0.006	0.010
6	4	S	-0.017	0.079	0.073	-0.042	-0.126	-0.062	0.003	-0.044	-0.035	-0.016	-0.039
6	5	C	0.194	0.209	0.076	0.155	-0.030	-0.069	-0.040	0.017	0.011	-0.017	-0.043
6	5	S	0.170	-0.113	-0.159	-0.039	-0.072	-0.018	-0.021	0.006	-0.008	-0.025	-0.018
6	6	C	-0.158	0.115	0.132	0.096	0.104	0.041	0.028	0.006	-0.019	-0.004	0.006
6	6	S	0.046	0.032	0.041	0.046	-0.009	-0.010	0.000	-0.003	-0.003	0.008	0.005

define the spherical harmonics by

$$Y_l^m(\theta, \varphi) = \left[(2-\delta_{mo}(2l+1)\frac{(l-m)!}{(l+m)!}\right]^{1/2} P_l^m(\cos\theta)\begin{pmatrix}\cos m\varphi \\ \sin m\varphi\end{pmatrix}$$

where $P_l^m(\cos\theta)$ is the associated Legendre polynomial.

The maps in Fig. 3(a–d) for the upper 1000 km of the mantle are similar to those in Tanimoto (1988) because of the dominance of surface wave data in the shallow depths. Two major features of that study, i.e. (1) velocity patterns in layer 1 correlate well with tectonics and age of the surface and (2) fast antipodal velocity anomalies in the western Pacific area and South America in the transition zone (layer 3), are seen in these maps. One should keep in mind, however, that due to the nature of the expansion (up to $l = m = 6$), small-scale features are lost in these maps.

In layer 5 (Fig. 3e), a fast-velocity anomaly is found from the northern part of the South America to the Caribbean, which seems to coincide with the finding by Grand (1986). Historically, a similar feature was first found by Jordan & Lynn (1974) and further studied by Lay (1983). In the same layer, we find a similar scale fast-velocity anomaly in the middle of the Pacific Ocean, a region near Saudi Arabia and the triple junction in the Indian Ocean. Thus a check of the present results can be done by a detailed regional study for those anomalies, similar to the work by Grand (1986) for North America. Further examination is important, since as we point out below there is a hint of aliasing effects for this result due mainly to the bad path coverage of data.

Dziewonski & Woodhouse (1987) reported the results of a similar *SH*-waveform inversion. They showed that a fast-velocity anomaly similar to Grand's (1986) can be traced to Canada and the Aleutian islands and suggested that they may be related to the subduction of old plates. A similar suggestion was made by Grand (1986) except that his anomaly does not extend to Canada. The results in Fig. 3e are consistent with the findings by Dziewonski & Woodhouse (1987) although their interpretation, that these anomalies are related to old, subducted slabs, is not established.

A common feature among layers in the lowermost mantle, starting at layer 8 or 9 and continuing to layer 11, is a fast-velocity feature which surrounds the Pacific Ocean. Areas under Alaska and also the western Soviet Union seem to have distinct large-scale fast anomaly for the lowermost two layers. These fast-velocity features around the Pacific Ocean generally agree with the results of Dziewonski & Woodhouse (1987). Their locations may suggest the connection of those fast-velocity anomaly to old subducted slabs. They also correspond well to where the continents are (except part of Africa). We should point out, however, that there seems to be two distinctly different types of structure obtained near the core–mantle boundary (CMB). The results in this paper agree well with another *SH*-waveform study by Woodhouse (as reported in Dziewonski & Woodhouse 1987) and an ISC study by Morelli & Dziewonski (1987). Two other studies by Creager & Jordan (1986) and Clayton & Comer (1983, private communication), both based on ISC data, show somewhat different patterns but seem to have similar features with each other. It seems that further careful study based on different data sets is required. We note that free oscillation studies (Ritzwoller *et al.* 1986; Giardini *et al.* 1987), although they tend to represent wider vertical averaging, produce similar patterns to the results in this paper in the lower mantle.

Although some similarities exist between this study and that by Dziewonski & Woodhouse (1987), there are some differences; one of the differences is found beneath South Africa where Dziewonski & Woodhouse (1987) found the velocity to be fast (or upward deformation of the CMB). They suggested a connection between this anomaly and a patch in the magnetic field (e.g. Bloxham & Gubbins 1987). However, we find the opposite (slow) velocity in this region.

If one examines the maps such as fig. 10 in Dziewonski & Woodhouse (1987), slow velocity is found by PKP(BC) waves but PCP results indicate fast velocity. It seems that further clarification of seismic results is required before comparisons to other data sets are made.

There is also another difficulty in interpreting the results for layer 11 because of the trade-off between velocity anomaly and boundary (CMB) perturbation. In terms of boundary deformation, higher velocity in this map can be interpreted as upward deformation of CMB. The long-wavelength nature of waves used to study the structure (~300 km) does not allow us to distinguish between the two cases. This trade-off becomes a serious problem if one attempts to explain this anomaly by thermal effects; in general, faster than average velocity implies lower temperature. On the other hand, if the boundary is deformed upward it would imply excess heat is coming out of the core at this location and thus imply higher temperature. It is clear that separation of velocity anomaly from boundary deformation is important in interpretation but is difficult to do at the moment. Morelli & Dziewonski's (1987) idea of using reflected (PCP) and transmitted (PKP) waves seems promising, since they have opposite effects from boundary perturbations, but it needs further confirmation from other data, since CMB maps among ISC studies do not presently agree (e.g. Creager & Jordan 1986; Morelli & Dziewonski 1987).

3.2 Resolution

Depth resolution for one of the spherical harmonic components ($l = m = 0$) is shown in Fig. 4. The thickness of each layer is approximately 250 km, thus the resolving length varies from about 200 km (top layer) to about 700–800 km (lower mantle). This is not as sharp as one would like but at least the peaks of the resolution kernel coincide with the desired layer number. Resolution kernels were obtained by using the method of Tanimoto (1988, section 4.2).

3.3 Depth distribution of power

In Fig. 5, we show the power of lateral heterogeneity as a function of depth. Power for the layer i, P_i, was calculated by

$$P_i = \frac{1}{2l+1}\sum_{m=-l}^{l}(b_{lm}^i)^2$$

where b_{lm}^i are the coefficients obtained in the inversion. In order to suppress the peak at the surface, they are divided

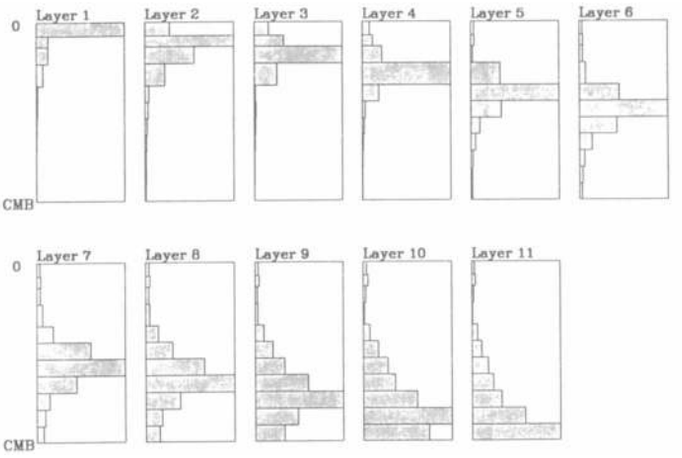

Figure 4. Resolution for each layer. Layer thickness is about 250 km. Thus half width of resolution varies from about 200 km at top to about 700–800 km in the lowermost mantle.

by the square of the radius (r^2). There is no physical meaning in this weighting scheme. Without this weight, the peak at the surface must be amplified by a factor of about 4 with respect to the one at the lowermost layer. It shows clearly a very unfortunate situation, in terms of obtaining the 3-D structure of the Earth; we observe that the relatively small heterogeneity in the deep interior is shielded to some extent by a very heterogeneous outermost layer.

In Fig. 5, aside from the peak at the surface, we see another peak in the lowermost mantle, layer 11 (CMB). The existence of this peak is not affected by the weight of $1/r^2$, since correction by $1/r^2$ for layer 10 and 11, for example, is not so different.

Care should be taken upon obtaining a result since a similar feature may arise if the data set does not have adequate coverage in the layer. This possibility can be excluded since the resolution given in Fig. 4 does not show such an anomalous feature for layer 11. In order to make sure, the path coverage for layer 11 is shown in Fig. 6. It seems that we have sufficient coverage over a large portion of the Earth in this layer.

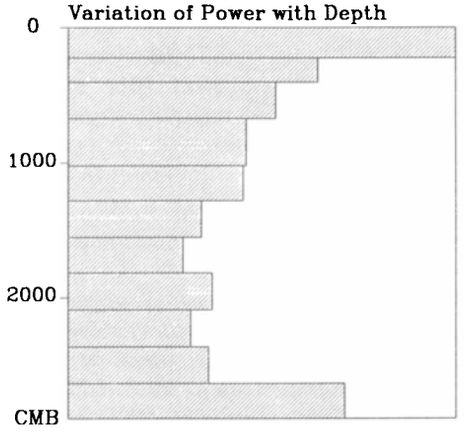

Figure 5. Power of lateral heterogeneity versus depth. This is normalized by $1/r^2$. There is clearly a very heterogeneous layer at the top of the mantle. The lowermost layer (D″) is also quite heterogeneous.

3.4 Dominance of $l = 2$ component

Figure 7 shows power distributions for angular orders 1–6 in each layer. The power of $l = 2$ is the largest for all layers except for the layer 5 (1000–1300 km). Although the dominance of $l = 2$ in the transition region was first shown by Nasters *et al.* (1982), our results suggest that this feature persists for the entire mantle.

A question which arises from Fig. 7 is that of the effect of aliasing. In general, based on our numerical experiences, a completely aliased result is occurring when the largest angular order (in this case $l = 6$) has a large amplitude. In this light, we may be able to say that the layers 1–3 and the layers 7–11 suffer little from aliasing effects. However, for the intermediate layers 4–6, there may exist some problems. Thus these results, especially the features in layers 4–6, may have to be examined with different data sets and methods. The real problem is, however, that there is no clear-cut way to examine whether a particular result suffers from aliasing or not.

4 LIMITATION OF THE THEORY

In view of the recent developments of the theory (Mochizuki 1986; Park 1987; Romanowicz & Roult 1986), the limitations of the method in this paper should be pointed out. In the following, we will present the kernels, which show the way that various waves (S, SS, $\cdots$) sample the mantle, using the (approximate) method described previously. The shape of those kernels, in principle, will show the shortcomings of the method in an explicit way.

Kernels are functions of three (spatial) coordinates but since it is rather difficult to plot 3-D objects in an understandable way, we simply show the slice, i.e. the 2-D section, of the kernel along the source–receiver path. Equations for kernels based upon the theory in Section 3 are given by

$$K(r, \theta, \varphi) = \sum_q \frac{2l+1}{4\pi} R_q S_q K_q(r)$$

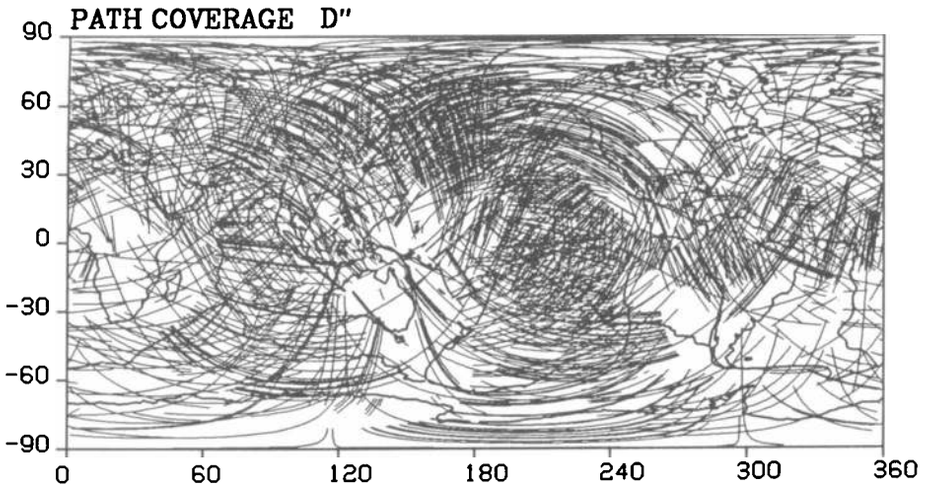

Figure 6. Path coverage in the lowermost layer (11).

where in the epicentral coordinate

$$R_q = -2\kappa_1 W(a)\cos(\varphi_{sr} - \varphi_{pr})P_l^{01}(\Delta_{rp})$$

$$S_q = 2\kappa_1 Z(r_s)(-M_{r\varphi}\cos\varphi_{sp} + M_{r\theta}\sin\varphi_{sp})P_l^{01}(\Delta_{sp}) + \frac{2\kappa_2 W(r_s)}{r_s}[2M_{\theta\varphi}\cos 2\varphi_{sp} - (M_{\theta\theta} - M_{\varphi\varphi})\sin 2\varphi_{sp}] \times P_l^{02}(\Delta_{sp})$$

where q is the index for a multiplet (n, l) and

$$\kappa_n = \frac{1}{2n}\sqrt{\frac{2l+1}{4\pi}\frac{(l+n)!}{(l-n)!}}.$$

Here W is the toroidal mode eigenfunction, a is the radius of the Earth and

$$Z = dW/dr - W/r.$$

φ_{sr} is the azimuth of source s observed at receiver r, φ_{sp} is the azimuth of source observed at a point p in the Earth, Δ_{rp} is the distance between receiver and a point P, and Δ_{sp} is the distance between source and p. Also, M_{ij} is the ij component of a moment tensor source and P_l^{mn} are generalized spherical harmonics defined by Phinney & Burridge (1973).

Figure 8(a, b) shows the results of computation for a source–receiver path of 90° and 150° respectively. The top trace is the radial variation of the kernel at the source location and the bottom is the kernel at the receiver location. In between, kernels at every 2° along the great circle path are shown. The left end is the surface and the right end is CMB. Due to the contributions from surface waves, amplitude of kernels near the surface become quite large. In order to show amplitude variation at depth, kernels shallower than 250 km are not shown here.

In Fig. 8(a), we can trace some of the body wave phases which sample the mantle. The direct *S*-wave kernel, near its turning point area, appears as small amplitude between the depth range of 2000 km and CMB and the distance range of 20° and 70°. Another small amplitude peak near 1300–1400 km, also between the distance range of 20° and 70°, corresponds to *SS*. Other multiple phases can be identified with even larger peaks at shallower depth. Similarly, various multiple phase paths are seen in Fig. 8(b).

One can immediately point out the problem from those figures; each body wave is most sensitive to its turning point regions and is elongated along the great circle path. Kernels for multiple *S* such as *SSS* and *SSSS* should have this type of elongation because of the nature of waves. But kernels for *S*

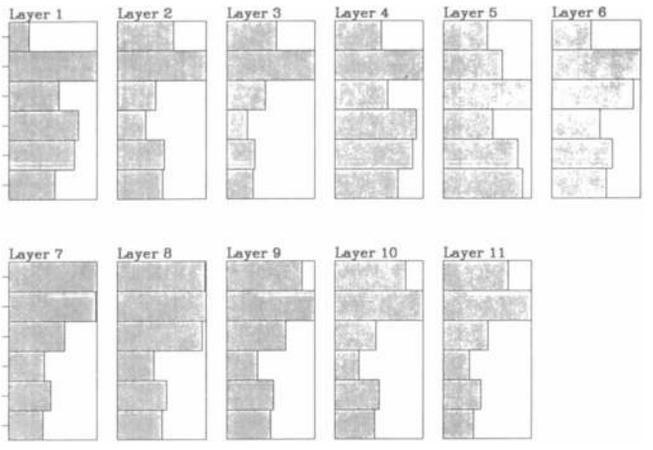

Figure 7. Power distribution of lateral heterogeneity (angular order 1–6) in each layer.

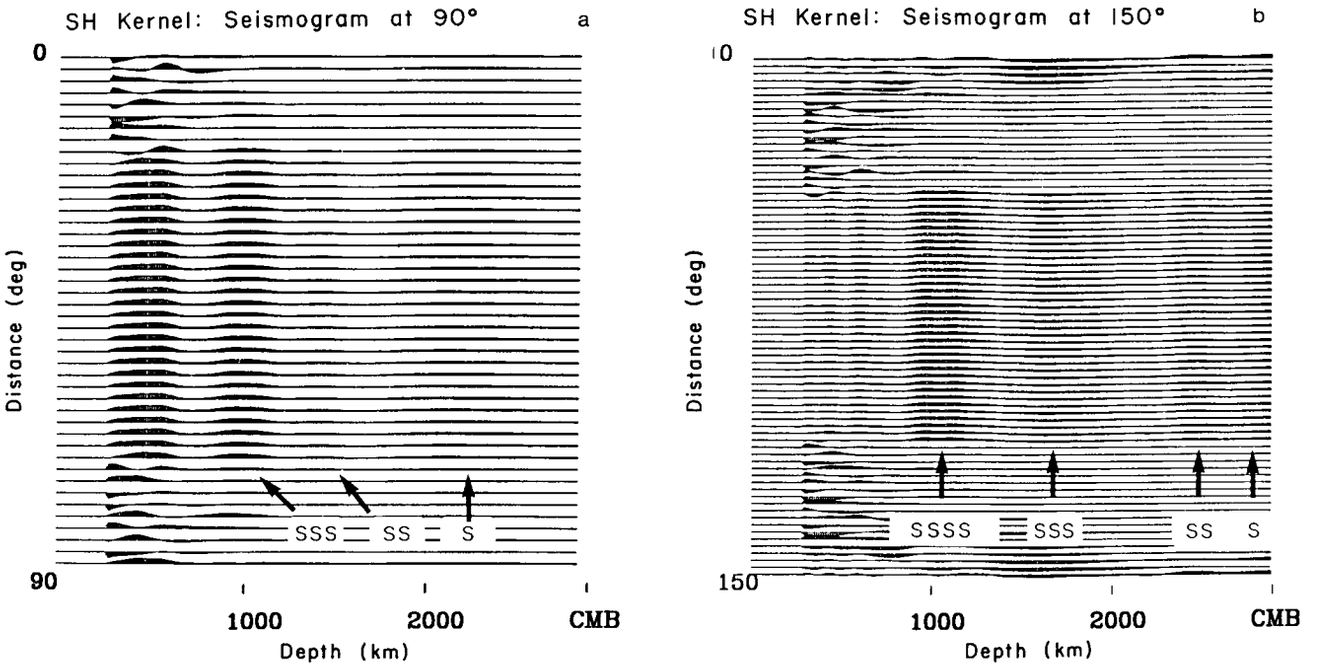

Figure 8. Slice of the kernels used for inversion. Distance is 90° for (a) and 150° for (b). The top trace is the radial variation of the kernel at the source and the bottom trace is the same at the receiver. The left end is the surface and the right end is the core–mantle boundary. Dark regions that can be vertically traced correspond to the turning point region of various phases: from right (deep) to left (shallow) they are *S* (diffracted), *SS*, *SSS*, · · · . Due to the nature of the approximation, elongation along the paths is seen for various phases.

and *SS* should show shapes closer to ray paths. These are caused by the nature of the approximation used in the theory. Elongation in the radius direction is caused by the relatively long wavelength of body waves used for this study.

However, we suggest that these shortcomings may not be so critical in retrieving the long wavelength anomaly using relatively short path (source–receiver) data. Since most of the paths have a short path length in each layer, and we are seeking very long wavelength anomaly (~5000 km), the effect of elongation cannot be so large. There is no doubt that we can improve the results by using a better theory, but considering the economy of the method and available computing power, the method in this paper may be a good compromise at the moment.

5 CONCLUSIONS

Using approximately 6000 long-period (40–100 s) *SH* body wave data and 1100 Love wave (100–500 s) data, we retrieved the long-wavelength (angular order 1–6) variation of the shear wave velocity structure in the mantle. The main conclusions are as follows.

(1) Patterns of (fast and slow) velocity anomalies in the top layer correlate with age and tectonics of the surface geology.

(2) In the depth range of 400–1000 km, we find two antipodal fast-velocity anomalies, one in the western Pacific and the other in South America. Both are in subduction zones and together form an $l = 2$ pattern.

(3) In layer 5 (1000–1300 km), a fast-velocity anomaly is found from the northern part of South America to the Caribbean. Although with diminishing amplitudes, thus with less certainty, this feature could be traced to Canada to the Aleutians.

(4) In the same layer, other anomalies are found in the middle of the Pacific and also in the Indian Ocean. Careful study in these areas will provide a check on this study.

(5) Depth distribution of lateral heterogeneity, in terms of its power, shows a strong peak at the surface and also a secondary peak at the bottom of the mantle (D″). The peak at the surface is quite large and points out an unfortunate situation for understanding the interior structure of the Earth. We have to deal with the small heterogeneity of the deep interior shielded by a very heterogeneous top layer. The peak at the bottom confirms the existence of a thermal and possibly chemical boundary layer there (D″).

(6) The $l = 2$ component of heterogeneity is the largest, except for layer 5 (1000–1200 km).

(7) In the lowermost mantle, a fast-velocity feature that surrounds the Pacific Ocean is found. This may be related to the thermal and chemical state of this layer, but its interpretation is difficult due to the trade-off between velocity anomaly and boundary perturbation.

ACKNOWLEDGMENT

This research has been supported by the NSF grant, EAR 8618759. I thank Don L. Anderson, Ed Garnero and Joanne Yoshimura for reading the manuscript. Contribution number 4639, Division of Geological and Planetary Sciences, California Institute of Technology, Pasadena, California, 91125.

REFERENCES

Bloxham, J. & Gubbins, D., 1987. Thermal core–mantle interactions, *Nature*, **325**, 511–573.

Creager, K. & Jordan, T., 1986. Aspherical structure of the core

mantle boundary from PCP travel times, *Geophys. Res. Lett.*, **13,** 1497–1500.

Dziewonski, A. & Anderson, D. L., 1981. Preliminary reference Earth model, *Phys. Earth planet. Inter.*, **25,** 297–356.

Dziewonski, A. M. & Woodhouse, J. H., 1987. Global images of the Earth's interior, *Science,* **236,** 37–48.

Giardini, D., Li, X. & Woodhouse, J. H., 1987. Three dimensional structure of the Earth from splitting in free oscillation spectra, *Nature,* **325,** 405–411.

Grand, S. P., 1986. Shear velocity structure of the mantle beneath the North American Plate, *PhD thesis,* California Institute of Technology, Pasadena.

Jordan, T. H. & Lynn, W. J., 1974. A velocity anomaly in the lower mantle, *J. geophys. Res.*, **79,** 2679–2685.

Lay, T., 1983. Localized velocity anomalies in the lower mantle, *Geophys. J. R. astr. Soc.*, **72,** 483–516.

Masters, G., Jordan, T. H., Silver, P. G. & Gilbert, F., 1982. Aspherical earth structure from fundamental spheroidal mode data, *Nature,* **289,** 609–613.

Mochizuki, E., 1986. Free Oscillations and surface waves of an aspherical Earth, *Geophys. Res. Lett.*, **13,** 1478–1481.

Morelli, A. & Dziewonski, A., 1987. Topography of the core–mantle boundary and lateral heterogeneity of the inner core, *Nature,* **325,** 678–683.

Nataf, H. C., Nakanishi, I. & Anderson, D. L., 1984. Anisotropy and shear-velocity heterogeneities in the upper mantle, *Geophys. Res. Lett.*, **11,** 109–112.

Nataf, H. C., Nakanishi, I. & Anderson, D. L., 1986. Measurements of mantle wave velocities and inversion for lateral heterogeneities and anisotropy. 3. Inversion, *J. geophys. Res.*, **91,** 7261–7307.

Park, J., 1987. Asymptotic coupled-mode expressions for nultiplet amplitude anomalies and frequency shifts on an aspherical earth, *Geophys. J. R. astr. Soc.*, **90,** 129–169.

Phinney, R. A. & Burridge, R., 1973. Representations of the elastic-gravitational excitation of a spherical earth model by generalized spherical harmonics, *Geophys. J. R. astr. Soc.*, **34,** 451–487.

Ritzwoller, M., Masters, G. & Gilbert, F., 1986. Observations of anomalous splitting and their interpretation in terms of aspherical structure, *J. geophys. Res.*, **91,** 10 203–10 228.

Romanowicz, B. & Roult, G., 1986. First order asymmetrics for the eigenfrequencies of the Earth and application to the retrieval of large-scale lateral variations of structure, *Geophys. J. R. astr. Soc.*, **87,** 209–239.

Tanimoto, T., 1984a. A simple derivation of the formula to calculate synthetic long-period seismograms in a heterogeneous earth by normal mode summation, *Geophys. J. R. astr. Soc.*, **77,** 275–278.

Tanimoto, T., 1984b. Waveform inversion of mantle Love waves: the Born seismogram approach, *Geophys. J. R. astr. Soc.*, **78,** 641–660.

Tanimoto, T., 1985. The Backus–Gilbert approach to the 3D structure in the upper mantle. I. Lateral variation of surface wave velocity with its error and resolution, *Geophys. J. R. astr. Soc.*, **82,** 105–123.

Tanimoto, T., 1986. The Backus–Gilbert approach to the 3D structure in the upper mantle II. SH and SV velocity, *Geophys. J. R. astr. Soc.*, **84,** 49–69.

Tanimoto, T., 1987. The three dimensional shear wave structure in the mantle by overtone waveform inversion I. Radial seismogram inversion, *Geophys. J. R. astr. Soc.*, **89,** 713–740.

Tanimoto, T., 1988. The 3D shear wave structure in the mantle by overtone waveform inversion II. Inversion of X waves, R waves and G waves, *Geophys. J. R. astr. Soc.*, **93,** 321–333.

Woodhouse, J. H., 1983. The joint inversion of seismic waveforms for lateral variations in Earth structure and earthquake source parameters, *Proceedings of the 'Enrico Fermi' International School of Physics LXXXV,* pp. 366–397, eds Kanamori, H. & Boschi, E.

Woodhouse, J. H. & Dziewonski, A. M., 1984. Mapping the upper mantle: three-dimensional modelling of earth structure of inversion of seismic waveforms, *J. geophys. Res.*, **89,** 5953–5986.